Lawrence Berkeley National Laboratory
LBL Publications

Title
Ferromagnetic resonators synthesized by metal–organic decomposition epitaxy

Permalink
https://escholarship.org/uc/item/14f0p5j6

Journal
Journal of Physics Condensed Matter, 35(48)

ISSN
0953-8984

Authors
Nguyen, Nhat
Herrington, Bryce
Chorazewicz, Kayetan
et al.

Publication Date
2023-12-04

DOI
10.1088/1361-648x/acf35b

Peer reviewed

Ferromagnetic resonators synthesized by metal-organic decomposition epitaxy

View the article online for updates and enhancements.

You may also like

- Electronic transport properties of spin-crossover polymer plus polyaniline composites with Fe3O4 nanoparticles
  Esha Mishra, Wai Kiat Chin, Kayleigh McElveen et al.

- Correlation effects and electronic structure of Gd@C_{60}
  R F Sabirianov, W N Mei, Jing Lu et al.

- The heteroisomeric diode
  Anthony N Caruso, Ravi B Billa, Snjezana Balaz et al.

Ferromagnetic resonators synthesized by metal-organic decomposition epitaxy

Nhat Nguyen[1] , Bryce Herrington[1], Kayetan Chorazewicz[2], Szu-Fan (Paul) Wang[3], Ruthi Zielinski[1], John Turner[4], Paul D Ashby[4] , Ufuk Kilic[5], Eva Schubert[5], Mathias Schubert[5], Ronald A Parrott[3], Allen A Sweet[3,6] and Robert Streubel[1,7,*]

[1] Department of Physics and Astronomy, University of Nebraska-Lincoln, Lincoln, NE 68588, United States of America
[2] University of California Berkeley, Berkeley, CA 94720, United States of America
[3] Vida Products Inc., Rohnert Park, CA 94928, United States of America
[4] Molecular Foundry, Lawrence Berkeley National Laboratory, Berkeley, CA 94720, United States of America
[5] Department of Electrical and Computer Engineering, University of Nebraska-Lincoln, Lincoln, NE 68588, United States of America
[6] Department of Electrical and Computer Engineering, Santa Clara University, Santa Clara, CA 95053, United States of America
[7] Nebraska Center for Materials and Nanoscience, University of Nebraska-Lincoln, Lincoln, NE 68588, United States of America

E-mail: streubel@unl.edu

CrossMark

Abstract

Metal-organic decomposition epitaxy is an economical wet-chemical approach suitable to synthesize high-quality low-spin-damping films for resonator and oscillator applications. This work reports the temperature dependence of ferromagnetic resonances and associated structural and magnetic quantities of yttrium iron garnet nanofilms that coincide with single-crystal values. Despite imperfections originating from wet-chemical deposition and spin coating, the quality factor for out-of-plane and in-plane resonances approaches 600 and 1000, respectively, at room temperature and 40 GHz. These values increase with temperature and are 100 times larger than those offered by commercial devices based on complementary metal-oxide semiconductor voltage-controlled oscillators at comparable production costs.

(Some figures may appear in colour only in the online journal)

---

* Author to whom any correspondence should be addressed.

1. Introduction

Information and communications technology consumes 800 TWh worldwide and sees an ever-growing data traffic that increases by a factor of one million every decade [1]. In order to enhance the rate of information transfer, channel bandwidth or signal power have to be increased, or noise power reduced. This leap in data rate will ultimately be accomplished with the next generation of cellular devices using radio frequencies between 24 and 70 GHz. To date, most equipment manufacturers and cellular network operators have encountered technical difficulty with implementing cellular in the $(24 \sim 28)$ GHz band and defaulted to a lower-frequency band, i.e. $(3.45 \sim 4)$ GHz [2], also evident from auctions by the Federal Communications Commission totaling $1 trillion [3–5]. This is mainly because modern technology uses complementary metal-oxide semiconductor (CMOS) voltage-controlled oscillators [6] that generate a considerable phase noise due to poor quality factors <5 which become worse at higher frequencies [7]. The quality factor [8] is the ratio of the resonator's stored energy to its dissipated energy per cycle at resonance and a measure for the oscillator's potential to generate phase noise [9]. Importantly, the quality factor is identical to the ratio of resonance frequency or field of the oscillator to the bandwidth of the generated signal [10]. A potent alternative is to design tunable oscillators [11] and bandpass filters [12] with yttrium iron garnet (YIG, $Y_3Fe_5O_{12}$) [13] and related garnets leveraging their outstanding magnetic characteristics. This materials class appeals not only to cellular communications, but also to magnonic electronics [14], transistors [15, 16], and logic gates [17] harnessing the inverse spin Hall effect [18–20] and spin pumping [21–24]. The synthesis of single-crystal films [25] is generally based on liquid-phase epitaxy [26, 27], pulsed laser deposition [19, 22, 28–32], and off-axis sputtering [33–38]—involving high-vacuum fabrication tools that lack scalability for high-volume manufacturing.

The high demand for tunable high-quality factor resonators led to commercial devices based on single-crystal YIG microspheres with a more complicated fabrication and integration process. Transitioning from YIG spheres to YIG nanofilms will simplify integration and lower the need for large magnetic bias fields, generated by either a permanent magnet or an electromagnet, due to different demagnetization factors and a planar-film relation between resonance frequency and magnetic field shifted toward higher resonance frequencies [39, 40]. Importantly, the transformation of a sphere (symmetric resonance) into a truncated hemisphere (excitation of higher modes on small-field side of main resonance) leaves the linewidth of the main resonance unaffected [40]. A similar effect should hold for thickness-modulated films. In pursuit of an economical synthesis of high-quality factor ferromagnetic resonators, we recently developed a wet-chemical approach based on metal-organic decomposition epitaxy to grow epitaxial YIG films [41].

Here, we report the temperature dependence of ferromagnetic resonances and associated physical quantities in YIG films synthesized by repeated metal-organic decomposition epitaxy. The homogeneity, surface roughness, local crystal lattice orientation, dielectric function, and film thickness are investigated by means of atomic force microscopy, electron backscatter diffraction, and spectroscopic ellipsometry. Magneto-optical magnetometry unveils a 1 mm-wide corner-/edge region with less optimal magnetic properties inherent to wet-chemical deposition and spin coating. The coexistence of sub-millimeter-sized single-crystal structures leads to multi-peak ferromagnetic resonance spectra, which are fitted using an appropriate number of symmetric and asymmetric Lorentzians to extract saturation magnetization, spin damping, magnetocrystalline anisotropy, Landé factor, and quality factor. This pragmatic approach is motivated by the need for micrometer-sized low-spin-damping materials in microelectronics resonator and oscillator devices.

2. Structural, optical, and static magnetic properties

The YIG films were synthesized using metal-organic decomposition from a FeY-03(5/3) precursor solution (Kojundo Chemical Laboratory Co., Ltd) [41, 42]. The solution containing 1.6 wt.% Fe_2O_3 and 1.4 wt.% Y_2O_3 was spin-coated (500 rpm for 10 s and 2000 rpm for 20 s) onto (5×5) mm^2 gadolinium gallium garnet(111) (GGG, $Gd_3Ga_5O_{12}$) substrates (purchased from University Wafer) and allowed to dry 24 h at room temperature and ambient conditions. Annealing at 1100 °C for four hours in a quartz tube furnace in oxygen atmosphere crystallizes the YIG film by decomposing the metal-organic compounds (pyrolysis), eliminating the remaining organic material, and promoting the atom migration to form the cubic YIG lattice structure according to the underlying GGG substrate (lattice constants: $a_{YIG} = 12.38$ Å; $a_{GGG} = 12.37$ Å). The structural film quality was quantified in terms of topography and relative crystal orientation using an Asylum Cypher Atomic Force Microscope and electron backscatter diffraction with a step size of about 10 μm in an FEI Strata 235 dual-beam Focused Ion Beam, respectively.

The resulting YIG monolayer film is atomically flat (figures 1(a) and (b)) and single-crystalline on the sub-millimeter length scale (figure 1(c)). Importantly, repeated spin coating and annealing to synthesize bilayer and trilayer films leave the crystallinity intact without signs of boundary layer discontinuity [41] or increased surface roughness corroborating homoepitaxial growth. The root mean squares for trilayer films is <0.3 nm compared with ≲0.35 nm for monolayers over an area of 4 μm^2. However, the most obvious difference in film quality for monolayer and trilayer emerges in the ferromagnetic resonance linewidth (discussed below). The extent to which this process or future refined procedures can be repeated without compromising film quality is unclear. Films prepared by seven repetitions of spin coating and annealing (seven-layer) possess worse properties due to texturing and percolation (figures 1(a)–(c)). Depending on the region of interest, i.e. with or without areas containing holes,
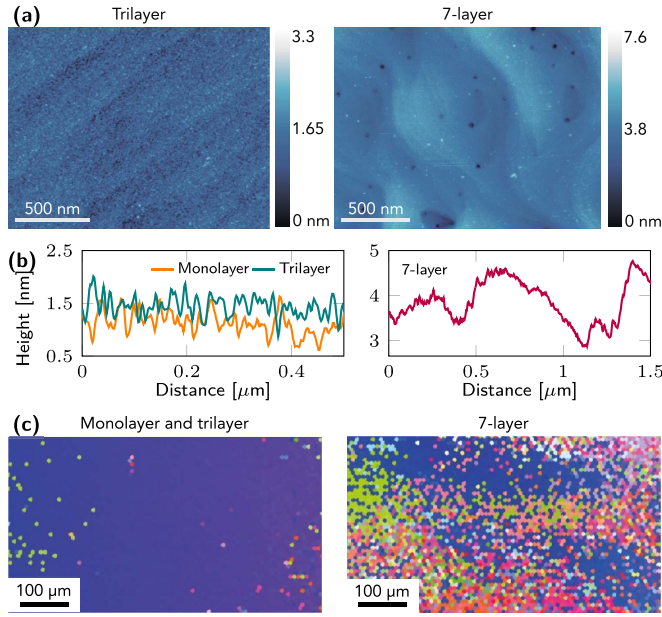
Figure 1. Structural properties of YIG nanofilms synthesized using metal-organic decomposition epitaxy. (a) Topography retrieved with atomic force microscopy unveiling atomically flat trilayers and percolated/decorated seven-layer films. (b) Representative line profiles for monolayer, trilayer, and seven-layer films corroborating similar quality for the thinner films. (c) Electron backscatter diffraction confirming epitaxial single-crystal growth of monolayers and trilayers on the sub-millimeter scale and polycrystalline texturing in seven-layer films.

Figure 2. Optical characterization of film thickness and magnetic hysteresis loops. (a) Real (ε_1) and imaginary (ε_2) components of dielectric function of YIG nanofilms obtained with spectroscopic ellipsometry. Spectral evolution of Mueller matrix elements of (b) YIG monolayer, (c) trilayer, and (d) seven-layer films. Experimental ellipsometry and modeled data are plotted as color and black curves, respectively. Deviations in the visible light range for seven-layer films originates from depolarization of the probe beam due to polycrystallinity. (e) Spatial dependence of room-temperature magnetic coercive field obtained with magneto-optical Kerr effect magnetometry expressed in terms of the distance from the corner of (5×5) mm^2 pieces. The vertical lines indicate the coercive field observed in all samples (regions) with presumably poor film quality.

the surface roughness is <1.2 nm or <0.6 nm over an area of 4 μm^2. Topographical steps in the size of the YIG cubic lattice constant [(1.2 ± 0.2) nm] occur on the sub-micrometer scale and likely coincide with the reorientation of the local lattice (figure 1(c)).

The change in structural and chemical order manifests in the optical, static and dynamic magnetic properties. Both real and imaginary parts of the dielectric function (figure 2(a)) were determined from spectroscopic ellipsometry [43] using multiple sample analysis [44, 45] without the need for band structure calculation to model the dielectric function or guess the latter. The reflected intensity was recorded with a charge-coupled device based spectroscopic ellipsometer with synchronized dual rotating compensator (RC2 by J.A. Woollam Co., Inc.) at various angles of incidence (45°, 55°, 65°, 75°) and in the spectral range (194 ~ 1240) nm. For isotropic systems, such as YIG(111) on GGG(111), additional angles of incidence do not provide further information but increase the signal-to-noise ratio, which was found to suffice. The spectral evolution of the complex reflectance ratio r_p/r_s of p- and s-polarized light is analyzed in terms of the Mueller matrix elements [46] using a commercial software (WVASE32 from J.A. Woollam Co., Inc.). The analysis relies on an ambient-layer(-layer)-substrate configuration and requires knowledge about the dielectric function of the GGG(111) substrate. The agreement between experimental and modeled Mueller matrix elements for monolayers and trilayers is remarkable and underlines their crystal quality (figures 2(b) and (c)). The
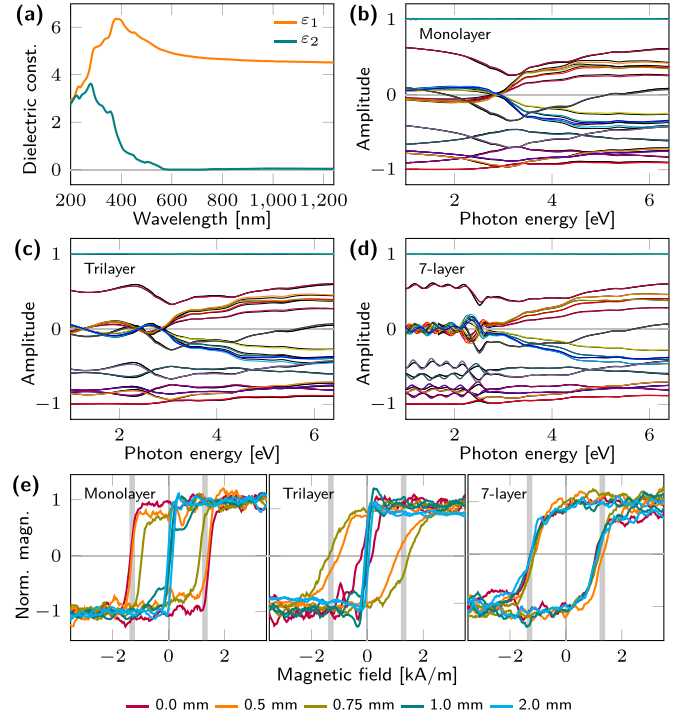
polycrystallinity of seven-layer films (figure 1(c)) causes slightly worse behavior evident in the visible light range due to depolarization of the probe beam (figure 2(d)). Assuming the same dielectric function for monolayer, trilayer, and seven-layer films, the film thickness could be quantified with sub-nm resolution. The extracted film thickness for monolayer [(41.49 ± 0.08) nm], trilayer [(129.63 ± 0.11) nm], and seven-layer [(279.99 ± 0.05) nm] films coincide with previously reported x-ray diffraction-based values [41] but are two orders of magnitude more precise.

Using magneto-optical Kerr effect magnetometry [47] with a spatial resolution <0.5 mm allowed for probing the magnetization reversal process, i.e. magnetic hysteresis loop and coercive field (figure 2(d)). The displayed curves are averaged over 500 consecutive scans owing to the weak Kerr signal in oxides for red light (639 nm continuous-wave diode laser) (figure 2(a)) despite intensity modulation at 1.4 kHz (probe) and 1.68 kHz (reference) with a mechanical chopper and dual-phase lock-in amplification (Stanford Research SR830). The hysteresis loops reveal a strong dependence of the coercive field on the distance from the corner and edge. This correlation is likely due to the inevitable thickness gradient

characteristic to spin-coated films and associated poorer crystallization. In monolayer and trilayer films, the edge region is less than 1 mm in width and marked by an abrupt, non-continuous transition from a perfectly soft central area with vanishing coercive field to a stepwise increase in coercive field up to 1.3 kA m^{-1}. The latter corroborates the existence of sub-millimeter-sized single-crystal films. While monolayer films possess rectangular hysteresis loops, trilayers feature slanted flanks with the same coercive fields near the corner. The same slanting is observed in seven-layer films. However, the seven-layer films are homogeneous on the sub-millimeter length scale with a coercive field matching that of the edge regions in monolayers and trilayers (figure 2(d)). These observations are consistent with the spatial variation of the lattice orientation (figure 1(c)) likely to cause grain boundary domain wall pinning. Both structure and magnetometry analysis suggests the occurrence of multiple ferromagnetic resonances in the spectra since corner/edge and central regions exhibit distinct coercive field, film thickness, and saturation magnetization.

3. Ferromagnetic resonance spectroscopy

The ferromagnetic resonances up to 40 GHz were probed via broadband spectroscopy in the temperature range (100 ∼ 370) K using a CryoFMR (NanOsc Instruments) inside a DynaCool Physical Properties Measurement System (Quantum Design). The samples were placed face-down on a coplanar waveguide that probes an area of roughly 1 mm^2 along its 250 μm-wide conductor. To enhance sensitivity, the field derivative of the absorption intensity, also known as the power absorption derivative dP/dH, was detected using a constant-frequency excitation field via two Helmholtz coils and sweeping the dc magnetic bias field H across the resonance. Each spectrum is fitted with a set of m derivatives of the sum of symmetric (L_i^{sym}) and asymmetric (L_i^{asym}) Lorentzians to isolate contributions from regions, e.g. central and edge regions, with different structural and magnetic properties. Simultaneously, this approach allows to extract the resonance fields H_{res}^i, intensities, and full widths at half maximum (FWHM) ΔH_i [48]:

$$\frac{\mathrm{d}P}{\mathrm{d}H} = \sum_{i=1}^{m} \left[a_i \frac{\mathrm{d}L_i^{\mathrm{sym}}(H)}{\mathrm{d}H} + b_i \frac{\mathrm{d}L_i^{\mathrm{asym}}(H)}{\mathrm{d}H} \right],$$

$$L_i^{\mathrm{sym}}(H) = \frac{\left(\frac{1}{2}\Delta H_i\right)^2}{-\left(\frac{1}{2}\Delta H_i\right)^2 + \left(H - H_{\mathrm{res}}^i\right)^2}, \quad (1)$$

$$L_i^{\mathrm{asym}}(H) = L_i^{\mathrm{sym}}(H) \cdot \frac{H - H_{\mathrm{res}}^i}{\frac{1}{2}\Delta H_i}.$$

The coefficients a_i and b_i describe the mixing of symmetric and asymmetric Lorentzians. The number of resonances m used to fit the spectra and their resonance magnetic field are indicated in each spectrum by vertical lines; the main resonance is highlighted by a reddish line. Analyzing the in-plane resonances in monolayer films reveals three distinct resonances (figure 3(a)) owing to spatial variations in coercive field, film thickness, and saturation magnetization (figure 1(c)). In
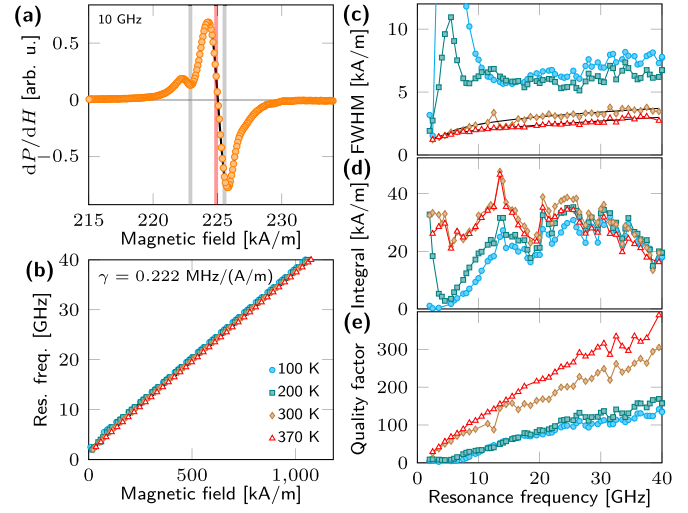

Figure 3. In-plane ferromagnetic resonances in YIG monolayers. (a) Spectrum taken at 300 K revealing one main resonance (reddish line) and two minor resonances (gray lines) that are fitted using a set of three derivatives of the sum of symmetric and asymmetric Lorentzians. (b) Dependence of the main ferromagnetic resonance on magnetic bias field exhibiting temperature-independent gyromagnetic ratio γ. (c) Full width at half maximum of main resonance, (d) integrated power absorption derivative, and (e) quality factor of main resonance. The non-linear dependence of the resonance width at high temperatures originates from two-magnon scattering. The sizable increase in resonance width at low temperatures and small fields coincides with the destructive interference of the coexisting resonances.

fact, all samples, except for the in-plane resonances in seven-layer films, require $m > 1$.

The relations between ferromagnetic resonance frequency and applied bias field $f_{\mathrm{res}}^{\parallel}(H)$ and $f_{\mathrm{res}}^{\perp}(H)$ for in-plane and out-of-plane geometry, respectively, are assembled to quantify the saturation magnetization M_s, the (isotropic) in-plane ($H_{\parallel}$) and perpendicular ($H_{\perp}$) magnetic anisotropy fields related to the respective anisotropies via $K = \frac{1}{2}\mu_0 M_s H$, and the gyromagnetic ratio $\gamma = g\mu_B/\hbar$ with the Bohr magneton μ_B and Landé factor g. This analysis is done with the main resonance. For in-plane spin precessions in a thin film, the relation reads [39, 49]:

$$2\pi f_{\mathrm{res}}^{\parallel} = \gamma\mu_0 \sqrt{(H_{\mathrm{res}}^{\parallel} + H_{\parallel})(H_{\mathrm{res}}^{\parallel} + H_{\parallel} - H_{\perp} + M_s)}. \quad (2)$$

The out-of-plane counterpart is [39, 49]:

$$2\pi f_{\mathrm{res}}^{\perp} = \gamma\mu_0 (H_{\mathrm{res}}^{\perp} - H_{\perp} - M_s). \quad (3)$$

In this notation, positive and negative $H_{\perp}$ refer to easy-axis and easy-plane anisotropy, respectively. The dominance of the main resonance (central region) over one, two, or multiple minor resonances (edge regions) is reflected by both amplitude and resonance field. In most cases, the extracted saturation magnetization and anisotropy fields of the main resonance are identical for any choice of m, including $m = 1$. The gyromagnetic ratio $\gamma = 0.222$ MHz (A m^{-1})$^{-1}$ is independent of film thickness, (main or minor) resonance, geometry, and temperature. The in-plane frequency-field relation is virtually linear

and approaches 40 GHz at H=1000 kA m^{-1} (figure 3(b)). It shifts toward smaller dc bias fields with decreasing temperature due to increasing saturation magnetization.

Other application-relevant materials properties, such as the Gilbert spin damping constant α, inhomogeneous line broadening ΔH_0, and frequency and temperature dependence of the quality factor Q [8], are retrieved from the FWHM resonance linewidth of the main resonance:

$$\Delta H = \Delta H_0 + 4\pi \alpha f / \gamma + \Delta H_\Gamma. \tag{4}$$

The quality factor is defined as the ratio of resonance field or frequency to the respective FWHM, i.e. $Q = H_{res}/\Delta H$ or $Q = f_{res}/\Delta f$ [10]. The third term on the right of equation (4) causes, for in-plane resonances, a strong non-linearity with the excitation frequency and describes the line broadening of uniform spin precession modes due to two-magnon scattering [50–54] on defects [55–57]:

$$\Delta H_\Gamma = \Gamma \sin^{-1} \sqrt{\frac{\sqrt{(f_{res}^{\parallel})^2 + f_M^2} - f_M^2}{\sqrt{(f_{res}^{\parallel})^2 + f_M^2} + f_M^2}}, \tag{5}$$

with $f_M = \gamma \mu_0 M_s / 2\pi$. The coefficient Γ weighs the two-magnon scattering contribution, which is for the investigated samples between 0.5 and 2. While the choice of m does not affect the frequency-field relation and related physical quantities, it has a notable influence on the linewidth of the main resonance. Its quality factor is 20% smaller for single-peak fitting compared with multi-peak fitting ($m = 3$). Moreover, linewidths retrieved from single-peak fits exhibit a pronounced non-linearity, which is strongly suppressed in case of multi-peak fitting. A clear two-magnon scattering contribution is only observed at 300 and 370 K (figure 3(c)). The partial destructive interference of the superimposed power absorption derivatives for low excitation frequencies prevents proper fitting of the low-temperature linewidth and determination of non-linear contributions. This cancelation is evident from the integrated power absorption derivative $\int \left| \frac{dP}{dH} \right| dH$, i.e. power absorption due to ferromagnetic resonance (figure 3(d)). It significantly broadens the linewidth (figure 3(c)) and, by extension, reduces the quality factor (figure 3(e)) at low frequencies and small bias fields. This has direct implications to the magnitude and uncertainty of the Gilbert damping. Hence, to accurately quantify the magnetic properties of individual single-crystalline regions, it is imperative to extrapolate linewidth and quality factor based on the frequency/magnetic field dependence of main and minor ferromagnetic resonances over a large range, e.g. 2–40 GHz. Aside from the discussed low-frequency deviations, the power absorption remains constant independent of the temperature up to 30 GHz and slightly declines for larger excitation frequencies (figure 3(d)). The dip around 18 GHz is due to the coplanar waveguide transmission amplitude and appears in all spectra.

4. Thickness dependence of ferromagnetic resonances

Although the film thickness changes by merely a factor of 3 from (41.49 ± 0.08) nm to (129.63 ± 0.11) nm, the trilayer films reveal a peak absorption signal that is 20 times larger for both in-plane and out-of-plane geometry than those observed in monolayers (figures 4(a) and (b)). Similar to the monolayer films, the power absorption for in-plane resonances is temperature- and nearly frequency-independent (figure 4(d)). For out-of-plane geometry, the ferromagnetic resonance intensity decreases with increasing frequency and matches the in-plane values near 10 GHz. Even at its lowest point, the sensitivity is larger than in monolayer films at any resonance frequency. The ferromagnetic resonances for in-plane geometry are with respect to the monolayer films shifted toward smaller dc bias field indicating a larger saturation magnetization (figure 4(c)). The improved crystal structure requires only double-peak fitting ($m = 2$) yielding a nearly linear increase of the linewidth with frequency for both high and low temperatures (figure 4(e)). Overall, the resonances are narrower and the high-temperature quality factor linearly increases with resonance frequency exceeding 600 for 40 GHz and $T \gtrsim 300$ K (figure 4(e)). At 100 K and high excitation frequencies, the quality factor settles in at 200; low-frequency spectra exhibit a broadened linewidth due to partial destructive interference, discussed above. Aside from 100 K, all in-plane quality factors exhibit the same temperature dependence in the entire frequency range $Q(f,T) = 1.5 \cdot [T/(1 \text{ K}) + 100] \cdot Q(f)/Q(40 \text{ GHz})$. The 100 K data are well described for resonance frequencies below 10 GHz owing to the two-magnon scattering contributions. Remarkably, the absorption peak intensity of out-of-plane resonances is even larger than those of the in-plane geometry because of a significantly smaller linewidth that is temperature-independent and, for frequencies $\gtrsim 20$ GHz, frequency-independent (figure 4(f)). This leads to an unprecedented quality factor exceeding 1000 at 40 GHz for operation temperatures between 200 and 370 K in spite of changing saturation magnetization and resonance field.

To augment these experimental data and explore the maximal quality factor possible at a reasonable resonance intensity, we performed micromagnetic simulations using Boris Computational Spintronics [58] and the Landau–Lifshitz-Gilbert formalism at 0 K on an NVIDIA Quadro RTX 8000. The materials parameters were chosen according to the room-temperature experimental data for trilayer films (figure 6): perpendicular magnetic anisotropy $K_\perp = -568$ J m^{-3} (in-plane), and $M_s = 136$ kA m^{-1}, $\alpha = 0.0005$, and $\gamma = 0.222$ MHz $(\text{A m}^{-1})^{-1}$ and Heisenberg exchange $J = 3.7$ pJ m^{-1} [26]. All films are modeled as a rectangular film (1 μm $\times$ 1 μm $\times$ t) with periodic boundary conditions along x and y axes and film thickness $t = 10, 60, 130$ and 200 nm. The mesh discretization along all three directions is at least half the magneto-static exchange length, i.e. $\frac{1}{2}\sqrt{A/(\frac{1}{2}\mu_0 M_s^2)} \approx 9$ nm. The ferromagnetic resonance spectra are obtained as the Fourier transform of the temporal evolution of the x-component of the magnetization following a pulse
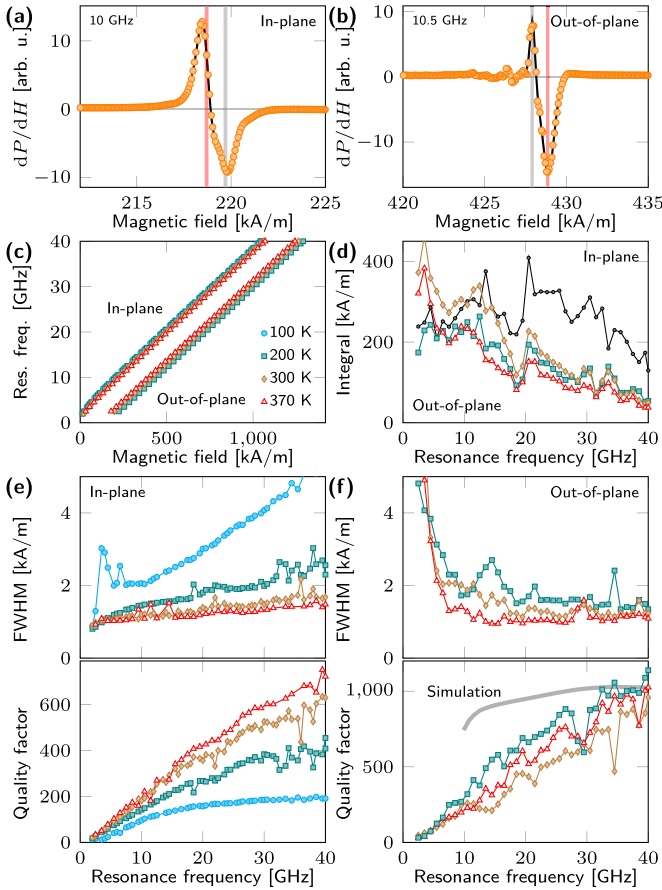
Figure 4. Ferromagnetic resonances in YIG trilayers obtained in in-plane and out-of-plane geometry. (a) In-plane and (b) out-of-plane ferromagnetic resonance spectra taken at 300 K consisting of two nearby resonances highlighted by vertical lines (reddish line refers to main resonance). (c) Dependence of the main ferromagnetic resonance frequency on applied bias field in in-plane and out-of-plane geometry with the same gyromagnetic ratio $\gamma = 0.222\,\mathrm{MHz\,(A\,m^{-1})^{-1}}$. (d) Integrated power absorption derivative for out-of-plane resonances highlighting decrease with resonance frequency. Black curve shows in-plane representative. (e), (f) Full width at half maximum and quality factor of main resonance in the presence of an (e) in-plane and (f) out-of-plane magnetic bias field. The quality factor at low temperatures is particularly enhanced in out-of-plane geometry approaching the 0 K value determined by micromagnetic simulations.

excitation $\mathrm{sinc}\{2\pi f_c(t - t_f/2)\}\,\mathrm{kA\,m^{-1}}$. The pulse is applied along x and perpendicular to the dc magnetic field (y for in-plane, z for out-of-plane). A simulation time $t_f = 100\,\mathrm{ns}$ and a cutoff frequency $f_c = 400\,\mathrm{GHz}$ are used to provide sufficient temporal and frequency resolution. Informed by the experimental data, the dc magnetic field is varied from $50\,\mathrm{kA\,m^{-1}}$ to $1500\,\mathrm{kA\,m^{-1}}$ in steps of $25\,\mathrm{kA\,m^{-1}}$. The linewidth of out-of-plane low-frequency/small-field resonances is enlarged in both numerical and experimental data. This suggests that superimposition of multiple resonances can occur even in perfect crystals without grain boundaries and defects. The modeled quality factor $Q = f_{\mathrm{res}}/\Delta f$ for out-of-plane resonances, expressed in terms of driving frequency, is film thickness-independent and, for high frequencies, frequency-independent (figure 4(f)).
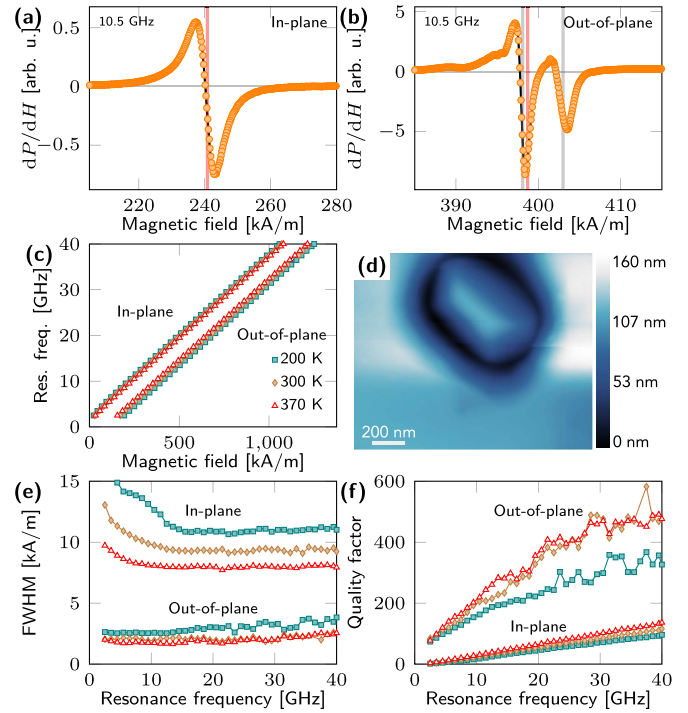
Figure 5. Comparison of ferromagnetic resonances in seven-layer films in the presence of in-plane and out-of-plane magnetic bias fields. (a) In-plane and (b) out-of-plane ferromagnetic resonance spectra taken at 300 K revealing broad distribution of resonance fields (polycrystallinity) and discrete field values, respectively. All frequency-field relations exhibit the same gyromagnetic ratio $\gamma = 0.222\,\mathrm{MHz\,(A\,m^{-1})^{-1}}$. Resonance fields are highlighted by vertical lines (reddish line indicates main resonance). (c) Dependence of the main resonance on magnetic bias field in in-plane and out-of-plane geometry. (d) Atomic force microscopy of frequently observed YIG grains that are likely the cause for the second high-field resonance in (b). (e) Full width at half maximum and (f) quality factor of main resonance showing significant enhancement in out-of-plane geometry owing to narrower and stronger absorption (a), (b).

While the experimental and numerical quality factors match at 40 GHz (≈ 1000), the linear increase of the experimental data with resonance frequency suggests the potential to outperform the modeled films at higher frequencies.

The polycrystalline structure of seven-layer films (figure 1(c)) yields a vast number of close localized resonances [57] that merge into one broad in-plane resonance (figure 5(a)). In contrast, triple-peak fitting ($m = 3$) is needed to properly capture the out-of-plane spectra (figure 5(b)) where uniform spin precessions can dephase without affecting those in adjacent regions. Aside from percolation, decoration, and texturing (figures 1(a) and (c)), the seven-layer films contain YIG islands in the form of pyramids with lateral expansions $(500 \times 750)\,\mathrm{nm}^2$ and height $>100\,\mathrm{nm}$ (figure 5(d)). The corresponding demagnetization factors of these embedded nanostructures are spatially dependent due to their curved shape and could vary by up to 200% ($\sim 10\,\mathrm{kA\,m^{-1}}$) [40], which is comparable with the magnetocrystalline anisotropy fields, causing a relation between ferromagnetic resonance and magnetic bias field that is distinct from continuous thin films.

This coexistence could explain the discrete set of out-of-plane resonances (figure 5(b)). The shoulder on the left side of the main resonance (smaller fields) is assigned to higher-order spin precession modes, including perpendicular standing spin wave resonances. In contrast to monolayer and trilayer films that exhibit small prominent resonances (figure 4(b)), the inhomogeneity and polycrystallinity of the seven-layer films give rise to a featureless shoulder that prevents a quantification of the exchange stiffness. The linewidth for in-plane and out-of-plane resonances are virtually frequency-independent for any temperature. In-plane resonances at low temperature reveal a larger inhomogeneous line broadening (offset) and an increased linewidth at low frequencies (figure 5(e)). The latter is likely due to partial destructive interference. The resulting quality factors increase linearly with the resonance frequency (figure 5(f)).

A quantitative comparison between monolayer, trilayer, and seven-layer films is given in figure 6. To illustrate the change in resonance amplitude, width, and shape, the power absorption derivatives at ≈ 10 GHz are plotted around their main resonance field for 300 K and in-plane and out-of-plane geometry (figure 6(a)). The experimental frequency-field relations are overlaid with numerical simulations revealing excellent agreement (figure 6(b)). Quantifying physical quantities, such as saturation magnetization, spin damping, inhomogeneous line broadening, and perpendicular and in-plane anisotropy, demonstrates superior materials properties of the trilayer films. This confirms the leading role of crystallographic order instead of film thickness, which is corroborated by micromagnetic simulations. The room-temperature value for the saturation magnetization of trilayer films (136 kA m^{-1}) (figure 6(c)), extracted using equations (2) and (3), is identical with the bulk value for YIG (140 kA m^{-1}) and films grown by liquid phase epitaxy [26, 27], pulsed laser deposition [19, 28, 31], and off-axis sputtering [35, 38, 59]. The saturation magnetization increases linearly with decreasing temperature in the temperature range $(200 \sim 370)$ K. Seven-layer films have expectedly a significantly smaller saturation magnetization. Surprisingly, the monolayers reach a magnetization of 140 kA m^{-1} only at 200 K. In contrast to trilayer and seven-layer films, the YIG monolayers unveil the same quality factor and linewidth for in-plane and out-of-plane resonances (figure 6(d)). The extracted inhomogeneous line broadening and Gilbert damping show a clear distinction between monolayer, trilayer, and seven-layer films (figure 6(e)). The large experimental uncertainty of the 200 K data for monolayers stems from the existence of multiple resonances that destructively interfere at low temperature preventing a differentiation by fitting (figure 3(c)). The given values are estimates obtained from the high-frequency regime with an inherently large fitting error. The perpendicular magnetic anisotropy of all samples ($K_\perp(300 \text{ K}) \approx -600$ J m^{-3}) (figure 6(f)) resembles the first-order cubic (in-plane easy-plane) anisotropy constant of YIG single-crystals $K = -610$ J m^{-3} [32, 60] and increases with decreasing temperature as the magnetocrystalline anisotropy increases ten-fold from 370 to 100 K [61]. The largest
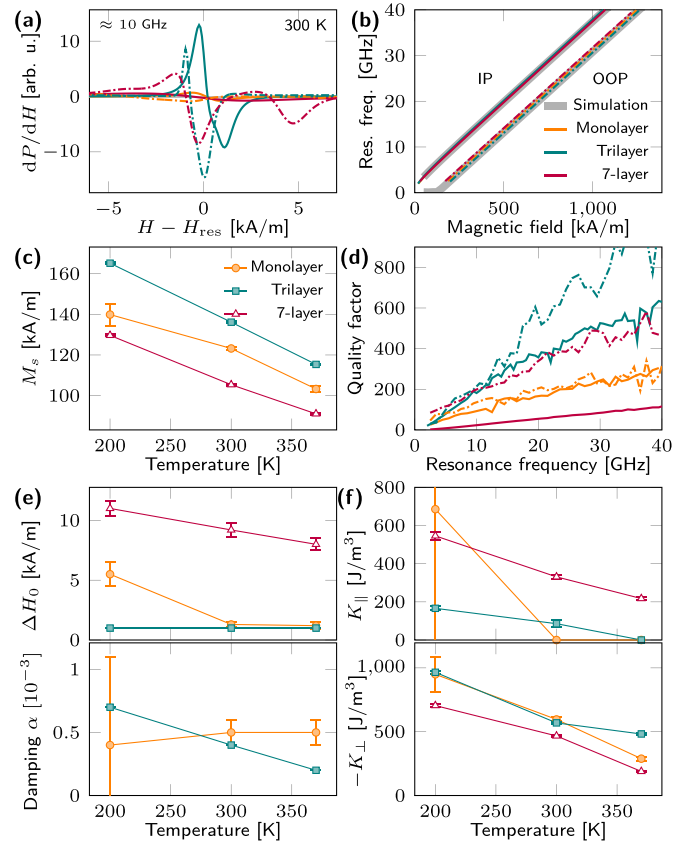

Figure 6. Materials parameters for monolayer, trilayer, and seven-layer films extracted from ferromagnetic resonance spectroscopy. (a) Spectra shifted around resonance field displaying shape, width, and magnitude differences of ferromagnetic resonances driven at ≈ 10 GHz and 300 K. (b) Corresponding frequency-field relations at 300 K with overlaid simulated values demonstrating leading role of structural/chemical order. (c) Saturation magnetization, (d) quality factor (300 K), and (e) inhomogeneous line broadening and Gilbert damping for in-plane resonances divulging superior properties of trilayer nanofilms. The large uncertainty of the Gilbert damping for monolayers at 200 K originates from the destructive inference of multiple resonances. (f) In-plane and out-of-plane magnetic anisotropy corroborating weak crystallographic anisotropy with a preferential in-plane easy-plane spin orientation. Solid and dash-dotted curves in (a), (b), and (d) refer to data obtained for in-plane and out-of-plane geometry, respectively.

deviation is observed for the seven-layer films, which possess similar in-plane and out-of-plane anisotropy values consistent with a cubic anisotropy. The in-plane anisotropy of monolayer and trilayer films is significantly smaller and is directly correlated with the inhomogeneous line broadening. For trilayers, the latter is <1 kA m^{-1}. Both Landé factor and gyromagnetic ratio are the same in all samples, at all temperatures, and both geometries indicating the same crystal cubic symmetry and spin–orbit coupling in in-plane and normal direction that does not change in the investigated temperature range. The non-vanishing anisotropy energy at 300 K is consistent with MOKE magnetometry that

unveiled slanted hysteresis flanks for trilayer and seven-layer films.

In conclusion, the YIG nanofilms synthesized by metal-organic decomposition epitaxy are soft-magnetic, low-spin-damping materials that can function as ferromagnetic resonators up to 40 GHz in both in-plane and out-of-plane geometry. Each deposited layer is roughly 40 nm thick yielding (41.5 ± 0.1) nm-thick monolayers, (129.6 ± 0.1) nm-thick trilayers, and (280.0 ± 0.1) nm-thick seven-layer films. The saturation magnetization and magnetocrystalline anisotropy coincide with values for single-crystals and epitaxial films grown by liquid phase epitaxy, pulsed laser deposition, and sputtering. While the quality factor for in-plane resonances shows a temperature dependence due to two-magnon scattering, the out-of-plane quality factor is virtually temperature-independent and approaches 1000 at 40 GHz. The investigated YIG films possess a 100 times larger quality factor compared with commercial devices based on CMOS voltage-controlled oscillators. This is equivalent to a 40 dB phase noise advantage for any realistic operation and/or outdoor temperature, e.g. $(-75 \sim 100)$ °C, at comparable production costs. With respect to films grown by liquid phase epitaxy, pulsed laser deposition, and off-axis sputtering, the YIG nanofilms exhibit a slightly smaller quality factor with the advantage of relying on a scalable low-cost fabrication process suitable to synthesize submicrometer-thick films. The inhomogeneous line broadening and, hence, quality factor can be further enhanced using more expensive GGG(111) substrates with superior crystallographic order [41]. It is also possible to refine the synthesis procedure for thick film growth by lowering the annealing temperature to suppress texturing and percolation and increase the quality factor. The resonance frequency, currently defined by film thickness, can be tuned by an external magnetic bias field, temperature, nanostructuring, or crystalline order. In reference to microelectronics applications, the fine tuning of resonance frequency can be accomplished using a Peltier element for temperature control of the saturation magnetization.

Data availability statement

Any data that support the findings of this study are included within the article.

Acknowledgments

ORCID iDs

Nhat Nguyen https://orcid.org/0000-0002-1095-1585
Paul D Ashby https://orcid.org/0000-0003-4195-310X
Allen A Sweet https://orcid.org/0000-0002-1158-0157
Robert Streubel https://orcid.org/0000-0003-4783-892X

References

[1] Ericsson ConsumerLab 2019 *Five Ways to a Better 5G: Key Trends Influencing Consumer Adoption of 5G* (Ericsson ConsumerLab)
[2] Kronestedt F, Asplund H, Furuskär A, Kang D H, Lundevall M and Wallstedt K 2018 The advantages of combining 5G NR with LTE (available at: www.ericsson.com/4ac642/assets/local/reports-papers/ericsson-technology-review/docs/2018/etr-2018-09-5g-radiodeployment.pdf)
[3] Federal Communications Commission 2022 Wireless telecommunications bureau grants additional auction 105 licenses (available at: www.fcc.gov/document/auction-105-long-form-applications-granted-4)
[4] Federal Communications Commission 2022 Wireless telecommunications bureau grants additional auction 107 licenses (available at: www.fcc.gov/document/auction-107-long-form-applications-granted)
[5] Federal Communications Commission 2022 Wireless telecommunications bureau grants auction 110 licenses (available at: www.fcc.gov/document/auction-110-long-form-applications-granted)
[6] Sweet A A 1990 *MIC and MMIC Amplifier and Oscillator Circuit Design* (Artech House)
[7] Qin P, Xue Q and Che W 2023 *IEEE Microw. Mag.* **24** 63–81
[8] Green E I 1955 *Am. Sci.* **43** 584
[9] Kajfez D 2005 *Q-Factor* (Wiley)
[10] Selesnick I W 2011 *IEEE Trans. Signal Process.* **59** 3560–75
[11] Sweet A A and Parrott R 2014 A wide band, low phase noise, differential yig tuned oscillator *WAMICON 2014* pp 1–3
[12] Tsai C, Qiu G, Gao H, Yang L, Li G, Nikitov S and Gulyaev Y 2005 *IEEE Trans. Magn.* **41** 3568–70
[13] Schmidt G, Hauser C, Trempler P, Paleschke M and Papaioannou E T 2020 *Phys. Status Solidi* b **257** 1900644
[14] Kajiwara Y *et al* 2010 *Nature* **464** 262–6
[15] Chumak A V, Serga A A and Hillebrands B 2014 *Nat. Commun.* **5** 4700
[16] Chumak A, Serga A and Hillebrands B 2017 *J. Phys. D: Appl. Phys.* **50** 244001
[17] Khitun A, Bao M and Wang K L 2010 *J. Phys. D: Appl. Phys.* **43** 264005
[18] Ando K *et al* 2011 *J. Appl. Phys.* **109** 103913
[19] d'Allivy Kelly O *et al* 2013 *Appl. Phys. Lett.* **103** 082408
[20] Nakayama H *et al* 2013 *Phys. Rev. Lett.* **110** 206601
[21] Sandweg C W, Kajiwara Y, Chumak A V, Serga A A, Vasyuchka V I, Jungfleisch M B, Saitoh E and Hillebrands B 2011 *Phys. Rev. Lett.* **106** 216601
[22] Heinrich B, Burrowes C, Montoya E, Kardasz B, Girt E, Song Y Y, Sun Y and Wu M 2011 *Phys. Rev. Lett.* **107** 066604
[23] Burrowes C, Heinrich B, Kardasz B, Montoya E A, Girt E, Sun Y, Song Y Y and Wu M 2012 *Appl. Phys. Lett.* **100** 092403
[24] Rezende S M, Rodríguez-Suárez R L, Soares M M, Vilela-Leão L H, Ley Domínguez D and Azevedo A 2013 *Appl. Phys. Lett.* **102** 012402

[25] Palisaitis J, Vasiliauskas R and Ferro G 2008 *Physics of Advanced Materials Winter School* pp 1–16

[26] Klingler S, Chumak A, Mewes T, Khodadadi B, Mewes C, Dubs C, Surzhenko O, Hillebrands B and Conca A 2014 *J. Phys. D: Appl. Phys.* **48** 015001

[27] Onbasli M C, Kehlberger A, Kim D H, Jakob G, Kläui M, Chumak A V, Hillebrands B and Ross C A 2014 *APL Mater.* **2** 106102

[28] Sun Y, Song Y Y, Chang H, Kabatek M, Jantz M, Schneider W, Wu M, Schultheiss H and Hoffmann A 2012 *Appl. Phys. Lett.* **101** 152405

[29] Hauser C, Richter T, Homonnay N, Eisenschmidt C, Qaid M, Deniz H, Hesse D, Sawicki M, Ebbinghaus S G and Schmidt G 2016 *Sci. Rep.* **6** 20827

[30] Tang C, Aldosary M, Jiang Z, Chang H, Madon B, Chan K, Wu M, Garay J E and Shi J 2016 *Appl. Phys. Lett.* **108** 102403

[31] Balinskiy M, Ojha S, Chiang H, Ranjbar M, Ross C A and Khitun A 2017 *J. Appl. Phys.* **122** 123904

[32] Mendil J *et al* 2019 *Phys. Rev. Mater.* **3** 034403

[33] Glass H L 1976 *J. Cryst. Growth* **33** 183

[34] Wang H L, Du C H, Pu Y, Adur R, Hammel P C and Yang F Y 2013 *Phys. Rev. B* **88** 100406

[35] Liu T, Chang H, Vlaminck V, Sun Y, Kabatek M, Hoffmann A, Deng L and Wu M 2014 *J. Appl. Phys.* **115** 17A501

[36] Wang H L, Du C H, Pu Y, Adur R, Hammel P C and Yang F Y 2014 *Phys. Rev. Lett.* **112** 197201

[37] Chang H, Li P, Zhang W, Liu T, Hoffmann A, Deng L and Wu M 2014 *IEEE Magn. Lett.* **5** 1

[38] Jermain C L, Aradhya S V, Reynolds N D, Buhrman R A, Brangham J T, Page M R, Hammel P C, Yang F Y and Ralph D C 2017 *Phys. Rev. B* **95** 174411

[39] Kittel C 1948 *Phys. Rev.* **73** 155–61

[40] Geschwind S and Clogston A M 1957 *Phys. Rev.* **108** 49–53

[41] Wang S F P *et al* 2021 *Appl. Phys. Lett.* **119** 172405

[42] Ishibashi T, Kawata T, Johansen T H, He J, Harada N and Sato K 2008 *J. Magn. Soc. Japan* **32** 150–3

[43] Schubert M 1998 *Thin Solid Films* **313–314** 323

[44] Kilic U, Sekora D, Mock A, Korlacki R, Valloppilly S, Echeverría E M, Ianno N, Schubert E and Schubert M 2018 *J. Appl. Phys.* **124** 115302

[45] Kilic U, Mock A, Sekora D, Gilbert S, Valloppilly S, Melendez G, Ianno N, Langell M, Schubert E and Schubert M 2020 *Sci. Rep.* **10** 10392

[46] Fujiwara H and Collins R W 2018 *Spectroscopic Ellipsometry for Photovoltaics* vol 1 (Springer)

[47] Kerr J 1877 *Phil. Mag.* **3** 321

[48] Liu L, Moriyama T, Ralph D C and Buhrman R A 2011 *Phys. Rev. Lett.* **106** 036601

[49] Farle M 1998 *Rep. Prog. Phys.* **61** 755

[50] Lindner J, Lenz K, Kosubek E, Baberschke K, Spoddig D, Meckenstock R, Pelzl J, Frait Z and Mills D L 2003 *Phys. Rev. B* **68** 060102

[51] Woltersdorf G and Heinrich B 2004 *Phys. Rev. B* **69** 184417

[52] McMichael R and Krivosik P 2004 *IEEE Trans. Magn.* **40** 2–11

[53] Lenz K, Wende H, Kuch W, Baberschke K, Nagy K and Jánossy A 2006 *Phys. Rev. B* **73** 144424

[54] Emori S, Alaan U S, Gray M T, Sluka V, Chen Y, Kent A D and Suzuki Y 2016 *Phys. Rev. B* **94** 224423

[55] Arias R and Mills D L 1999 *Phys. Rev. B* **60** 7395–409

[56] Arias R and Mills D L 2000 *J. Appl. Phys.* **87** 5455–6

[57] McMichael R D, Twisselmann D J and Kunz A 2003 *Phys. Rev. Lett.* **90** 227601

[58] Lepadatu S 2020 *J. Appl. Phys.* **128** 243902

[59] Chang C and Sakdinawat A 2010 *Nat. Commun.* **5** 4243

[60] Hansen P 1974 *J. Appl. Phys.* **45** 3638–42

[61] Dillon J F 1957 *Phys. Rev.* **105** 759–60